Molecular Cell
Article

Dynamic Architecture of a Minimal RNA Polymerase II Open Promoter Complex

Barbara Treutlein,[1] Adam Muschielok,[1] Joanna Andrecka,[1] Anass Jawhari,[2] Claudia Buchen,[2] Dirk Kostrewa,[2] Friederike Hög,[2] Patrick Cramer,[2] and Jens Michaelis[1,3,*]
[1]Department of Chemistry and Center for Integrated Protein Science München, Ludwig-Maximilians-Universität München, Butenandtstr.11, 81377 Munich, Germany
[2]Gene Center and Department of Biochemistry, Center for Integrated Protein Science CIPSM, Ludwig-Maximilians-Universität München, Feodor-Lynen-Strasse 25, 81377 Munich, Germany
[3]Current address: Physics Department, Ulm University, Albert-Einstein-Allee 11, 89081 Ulm, Germany
*Correspondence: jens.michaelis@uni-ulm.de
DOI 10.1016/j.molcel.2012.02.008

SUMMARY

The open promoter complex (OC) is a central intermediate during transcription initiation that contains a DNA bubble. Here, we employ single-molecule Förster resonance energy transfer experiments and Nano-Positioning System analysis to determine the three-dimensional architecture of a minimal OC consisting of promoter DNA, including a TATA box and an 11-nucleotide mismatched region around the transcription start site, TATA box-binding protein (TBP), RNA polymerase (Pol) II, and general transcription factor (TF)IIB and TFIIF. In this minimal OC, TATA-DNA and TBP reside above the Pol II cleft between clamp and protrusion domains. Downstream DNA is dynamically loaded into and unloaded from the Pol II cleft at a timescale of seconds. The TFIIB core domain is displaced from the Pol II wall, where it is located in the closed promoter complex. These results reveal large overall structural changes during the initiation-elongation transition, which are apparently accommodated by the intrinsic flexibility of TFIIB.

INTRODUCTION

Transcription initiation at eukaryotic protein-coding gene promoters requires assembly of RNA polymerase (Pol) II with the general transcription factors (TFs) IIB, -D, -E, -F, and -H into the closed promoter complex (CC) (Boeger et al., 2005; Hahn, 2004; Roeder, 1996). Pol II, TFIIB, TFIIF, and the TFIID subunit TATA box-binding protein (TBP) suffice to form a minimal CC (Killeen et al., 1992). After CC formation, the DNA surrounding the transcription start site (TSS) is melted and inserted into the active center cleft of the polymerase. The resulting open promoter complex (OC) enables RNA synthesis, which triggers release of the general TFs and conversion of the OC to a stable elongation complex (EC). Formation of the CC and its transition to the OC and EC all require TFIIB. TFIIB binds the Pol II dock domain with its N-terminal zinc-ribbon (B-ribbon) domain (Bushnell et al., 2004; Chen and Hahn, 2003) and binds TBP, promoter DNA, and the Pol II wall with its C-terminal (B-core) domain, which comprises two cyclin folds (Nikolov et al., 1995). The region connecting the B-ribbon with the B-core forms two elements, the B-linker and B-reader, which apparently are involved in DNA opening (Kostrewa et al., 2009) and TSS selection (Cho and Buratowski, 1999; Pardee et al., 1998; Ranish et al., 1999), respectively. TFIIB is displaced upon EC formation (Pal et al., 2005).

Previous structural studies have elucidated transcription initiation and elongation. The crystal structures of Pol II and the EC are known (Armache et al., 2005; Cramer et al., 2001; Gnatt et al., 2001; Kettenberger et al., 2004; Wang et al., 2006). The architecture of the CC was derived by locating general TFs and promoter DNA on Pol II with the use of biochemical crosslinking (Chen and Hahn, 2003, 2004; Chen et al., 2007; Chen et al., 2010; Kim et al., 2000; Miller and Hahn, 2006). The crystal structure of the Pol II-TFIIB complex is known and led to models of the CC (Kostrewa et al., 2009; Liu et al., 2010). Models of the OC were also proposed based on the Pol II-TFIIB structure and known biochemical data but the structure of the OC remains unknown. The OC likely contains flexible regions because it could not be trapped crystallographically and also because conversion from the CC to the EC requires large conformational changes in DNA and general TFs.

To structurally analyze flexible Pol II complexes that are not amenable to X-ray analysis, we developed the use of single-molecule Förster resonance energy transfer (smFRET). smFRET allows the structural analysis of flexible complexes and observation of conformational changes because it can be used to obtain distance information between a single pair of dye molecules attached to the complex in real-time (Ha et al., 1996; Joo et al., 2008). By trilateration of several FRET-derived distances, a region of unknown position can be located with respect to known positions within a complex (Andrecka et al., 2008; Knight et al., 2005; Margittai et al., 2003; Mekler et al., 2002; Rasnik et al., 2004; Wozniak et al., 2008). However, experimental uncertainties affect the most likely positions and must be accounted for by computing a three-dimensional probability density function (PDF) for each position. Our recently developed Nano-Positioning System (NPS) computes such PDFs using X-ray

structures, smFRET data, and Bayesian parameter estimation (Muschielok et al., 2008). NPS analysis of yeast Pol II ECs revealed the position of the 5′-end of exiting RNA (Andrecka et al., 2008), the influence of TFIIB on RNA position (Muschielok et al., 2008), and the course of nontemplate and upstream DNA (Andrecka et al., 2009). NPS was recently extended to include a global data analysis, which improves localization accuracy (global NPS) (Muschielok and Michaelis, 2011). Further, NPS docking was developed, which allows for the docking of macromolecules with known structure.

Here, we used smFRET, global NPS analysis, and NPS docking to determine the molecular architecture of a minimal OC consisting of Pol II, promoter DNA, TBP, TFIIB, and TFIIF. We measured smFRET efficiencies between "antenna" dye molecules (antennas) attached to the upstream nontemplate DNA, the TATA box, TBP, and TFIIB, and several "satellite" dye molecules (satellites) attached to positions on the template DNA and Pol II that are known from crystallographic structures. The data allowed us to build a model of the minimal OC, which provides insights into the mechanism of transcription initiation.

RESULTS

Assembly of OCs with Labeled DNA and Factors

We assembled minimal OCs sufficient for promoter-dependent transcription in vitro (Pan and Greenblatt, 1994), composed of purified endogenous yeast Pol II-TFIIF complex, recombinant TBP, and recombinant TFIIB on a synthetic DNA scaffold with a mismatched region that mimicked the transcription bubble (see Experimental Procedures). The scaffold resembled in sequence the one used for X-ray structure determination of the complete Pol II EC (Kettenberger et al., 2004) but contained a TATA box 30 nt upstream of the TSS and an 11 nt mismatched region around the TSS from register −9 to +2, where +1 is the TSS and negative and positive numbers denote upstream and downstream positions, respectively (Figure 1A). In the scaffold, the point of strand separation is located 20 bp downstream of TATA, which corresponds to the distance where DNA opening commences in yeast and human (Giardina and Lis, 1993; Wang et al., 1992).

We attached satellites to one of three positions on the downstream template DNA (T-DNA[+3], [+7] or [+12]) or to one position on the upstream template DNA (T-DNA[−10]), or to residue C150 of a single-cysteine mutant of the Pol II subunit Rpb7 (Experimental Procedures and Figure S1 available online). We placed antennas on three different elements of the OC, namely the TBP-TATA DNA complex, upstream DNA, and TFIIB (Figures 1A and 1B). TBP-TATA was labeled on one of two positions on the TATA box (NT-DNA[−30] or [−23]) or on residue C128 of TBP (TBP-C128). The upstream DNA contained one antenna at position −18 of the nontemplate DNA (NT-DNA[−18]). TFIIB was labeled with a Sfp phosphopantetheinyl transferase-catalyzed strategy (Yin et al., 2006) that required insertion of an 11-amino acid ybbR-tag into an unstructured region of the protein. We introduced labels adjacent to the N-terminus of TFIIB cyclin 1 (TFIIB-[122]ybbR) and in the TFIIB C-terminal tail (TFIIB-[C-term]ybbR).

We verified that introduction of a ybbR-tag into TFIIB did not impair transcriptional activity by performing an in vitro transcription assay using nuclear extract from a temperature-sensitive yeast strain carrying a point mutation in the TFIIB gene (Ranish et al., 1999) (Supplemental Experimental Procedures). Such extracts do not support transcription, but promoter-dependent transcription was recovered when recombinant wild-type TFIIB or one of the two TFIIB-ybbR mutants were supplied (Figure S2A). We used an electrophoretic mobility shift assay to demonstrate that fluorescently labeled DNA and proteins assembled into stable OCs (Figures S2B and S2C).

Downstream DNA Occupies the Cleft

Assembled OCs were purified by size-exclusion chromatography, attached to the surface of microfluidic chambers, and investigated by smFRET using total internal reflection fluorescence microscopy (Experimental Procedures and Supplemental Experimental Procedures). The location of the satellites on the downstream template DNA and the template strand in the bubble was assumed to resemble that in the EC (Kettenberger et al., 2004), consistent with mutagenesis data (Kostrewa et al., 2009) and with a crystal structure of Pol II in complex with free DNA (Cheung et al., 2011). To test this, we measured smFRET between satellites on the template DNA (T-DNA[−10], [+3] or [+7]) as donors and satellite Rpb7-C150 as acceptor for both OC and EC (Figure 2 and Tables S1 and S2). For the EC, all three measurements resulted in smFRET efficiency histograms showing a single peak. For the OC, the FRET efficiency histogram for the measurement between upstream satellite T-DNA(−10) and Rpb7-C150 resembles the corresponding histogram for the EC, indicating that the position of the upstream template strand in the bubble is not altered. smFRET measurements for the two downstream template DNA satellites T-DNA(+3) and T-DNA(+7) in the OC resulted in bimodal FRET efficiency distributions with two distinct, comparatively narrow peaks that can be fitted with two Gaussian distributions, comprising 70% and 30% of the data. The main peak of the distributions resembles the single peak of the EC, indicating that in the major population of OCs the downstream DNA adopts a location in the polymerase cleft similar to that in the EC.

Dynamic DNA loading into the Cleft

In the above experiments, a subpopulation of OCs with a high FRET efficiency was also observed, indicating an alternative location of the downstream DNA. Similar observations were made in smFRET measurements from satellites to the antennas positioned on the upstream DNA (NT-DNA[−18], [−23], or [−30] Figures 3 and S3). For all downstream satellites (Figures 3D, 3E, and 3F), two Gaussians are necessary to describe the data. The side peaks corresponding to a subpopulation of OCs of about 30% are located at higher FRET efficiencies, indicating that the alternative location of downstream DNA is closer to Rpb7 and upstream DNA. Side populations were also observed in measurements between downstream satellites and antennas on TBP or TFIIB (e.g., Figure S5D); however, these data were not included in the following NPS analysis due to comparatively poor statistics. Global NPS analysis (see Experimental Procedures and Supplemental Experimental Procedures) using all

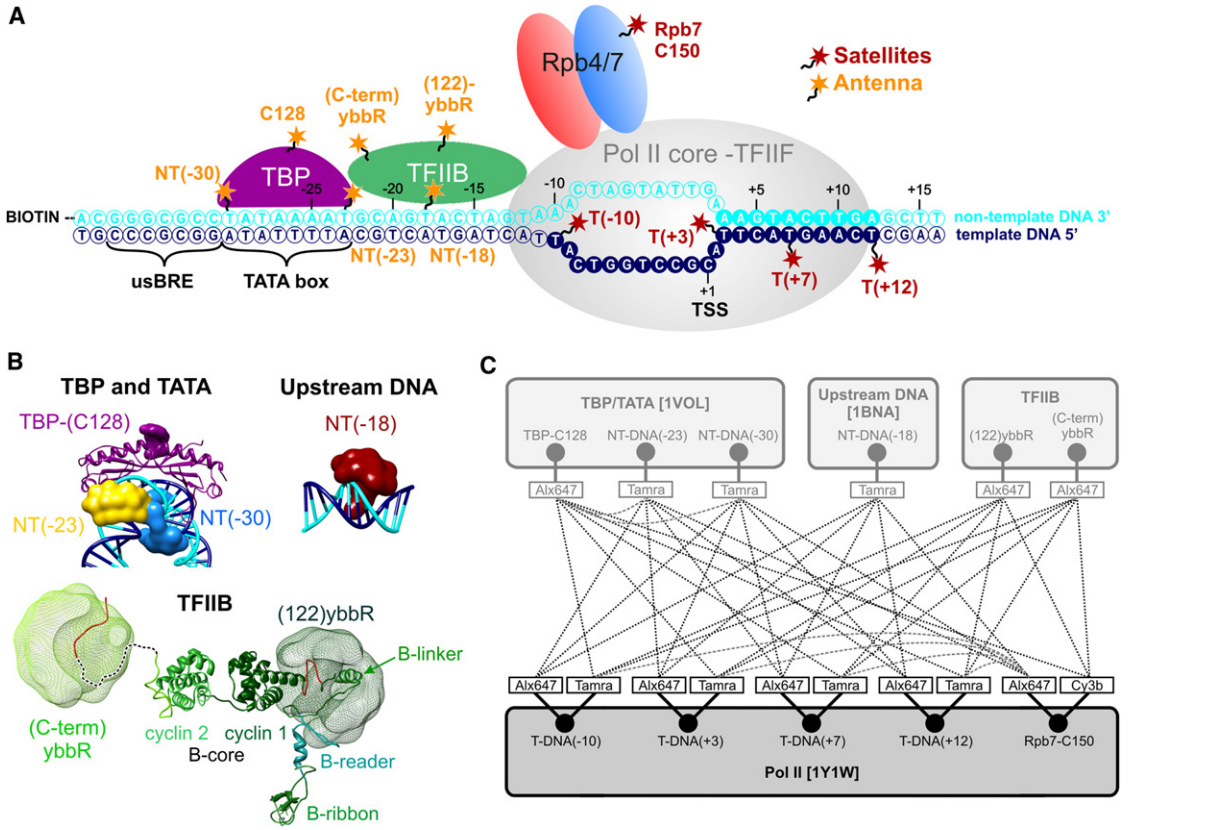

Figure 1. Experimental Design of a Minimal OC for Global NPS Analysis

(A) Cartoon illustrating nucleic acid scaffold and label positions. OCs were formed using artificially mismatched DNA scaffolds (T-DNA, blue; NT-DNA, cyan) containing a TATA box and an upstream TFIIB recognition element (usBRE). Bases whose positions can be inferred from the Pol II EC structure (Kettenberger et al., 2004) (pdb ID: 1Y1W) are shown as solid circles, whereas bases unresolved in the crystal structure are shown as open circles. Proteins constituting the minimal OC are shown schematically.

(B) Antenna position priors within their respective reference frame for TBP-TATA (pdb ID: 1VOL without TFIIB) (Nikolov et al., 1995) and the upstream DNA (pdb ID: 1BNA) (Drew et al., 1981). For illustration purposes of the antennas on TFIIB, the ybbR-tag (red) as well as the C-terminal tail of TFIIB with unknown structure (dashed line) were modeled in an arbitrary conformation into the TFIIB structure (Kostrewa et al., 2009) (pdb ID: 3K1F) using coot (Emsley et al., 2010). The dyes were attached via a linker to the second residue of the respective ybbR-tag and the modeled accessible volume of each dye given the modeled conformation of the C-terminal tail of TFIIB is presented as a meshed density. Images were prepared using Chimera (Pettersen et al., 2004). See Figure S1 for satellite position priors.

(C) Schematic representation of FRET network for NPS docking analysis of the OC. All satellites and antennas are shown in their respective reference frame together with the attached dye molecules. FRET efficiencies (n = 37) were measured between pairs of satellite and antenna dyes (dotted black lines) and in between satellites or antennas, respectively (dashed gray lines). The location and orientation of TBP-TATA and of antennas NT-DNA(−18), TFIIB-(122)ybbR and (C-term)ybbR (gray-hued) relative to the Pol II coordinate system (dark-hued) were to be determined by global NPS analysis (Muschielok and Michaelis, 2011).

side peaks in measurements between positions on the downstream DNA and on the upstream DNA or TATA DNA revealed that the alternative location of downstream DNA is on top of the cleft between the Pol II clamp and lobe that flank opposite sides of the cleft (Figure 4A).

smFRET time traces show a dynamic transition between the two downstream DNA locations in and above the cleft at a timescale of seconds (Figures 4B and 4C). For quantification of the data, we performed hidden Markov modeling (HMM) (Experimental Procedures). Due to the presence of two peaks in the FRET histograms, a two-state hidden Markov process was assumed. Analysis of 88 time traces undergoing 240 transitions resulted in a transition density plot (TDP, Figure 4D) that shows two distinct transitions from an initial FRET efficiency of around 80% to a final FRET efficiency of around 30% and vice versa. From the TDP, cumulative distributions for the dwell times of both transitions were extracted and fitted by monoexponential decays, which yielded the rates k_{out} = (0.8 ± 0.1) s^{-1} and k_{in} = (1.5 ± 0.4) s^{-1}, respectively. The ratio of the rates of movement in and out of the cleft is in good agreement with the respective FRET efficiency histogram (Figure S3K and Table S1), which shows a fraction of ~ 30% of all OCs in the high-FRET state with the downstream DNA above the cleft and a fraction of ~ 70% in the low-FRET state with the downstream DNA localized in the cleft.

TBP and TATA DNA Reside Above the Cleft

To determine the positions of upstream DNA, TBP, and TFIIB within the OC, we measured smFRET for all combinations of satellite and antenna pairs and for several combinations of two

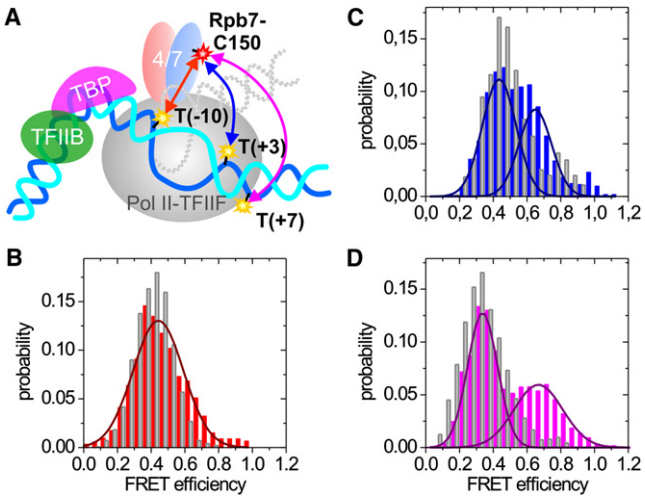

Figure 2. Localization of Satellites within OC

(A) Cartoon indicating the label positions and smFRET measurements for experiments designed to test whether the EC structure is a good model for the OC with respect to the position of the downstream template DNA and the template strand in the bubble. Measurements from satellite Rpb7-C150-Alexa647 to satellites T-DNA(−10)-Tamra (red arrow), T-DNA(+3)-Tamra (blue arrow) or T-DNA(+7)-Tamra (pink arrow) were performed in an OC as well as in an EC.

(B–D) Comparison of framewise smFRET histograms from OC measurements (color of histogram matching color of arrow in [A]) and EC measurements (gray histograms). Minor subpopulations are found for the downstream DNA satellites T-DNA(+3) and (+7) at substantially higher FRET efficiencies, which arise from an alternate conformation of the downstream DNA with a shorter distance to Rpb7-C150 (dotted gray lines in [A]).

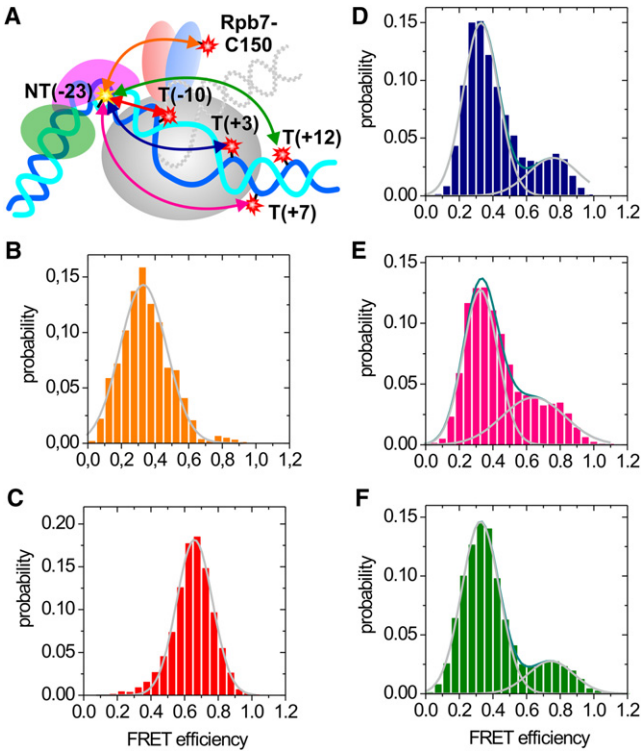

Figure 3. Downstream DNA in OC Adopts Two Different Conformations

(A) Cartoon illustrating an exemplary set of smFRET measurements from all satellites to an upstream DNA antenna position, namely the data for NPS localization of antenna NT-DNA(−23). The measurements are indicated by double-headed arrows in the same color as the respective FRET efficiency histogram in (B–F) (orange for satellite Rpb7-C150, red for T-DNA[−10], blue for T-DNA[+3], pink for T-DNA[+7], and green for T-DNA[+12]). An OC is presented schematically and the alternate conformation of the downstream DNA is sketched with dotted gray lines.

(B and C) smFRET measurements for the satellite positions on the *upstream* DNA resulted in FRET efficiency histograms, which were fitted with single Gaussians (gray).

(D–F) FRET efficiency histograms for measurements to the satellite positions on the *downstream* DNA were fitted with two Gaussians. (gray: individual fit, dark cyan: combined fits).

satellites or two antennas, yielding a total of 37 measurements (Figures 1C, S3, S4, and S5). We also measured fluorescence anisotropies of the donor and acceptor dyes for all attachment sites and experimentally determined the isotropic Förster distance for each acceptor and donor dye pair (Table S1). To apply NPS docking (Muschielok and Michaelis, 2011), we defined two rigid macromolecular structures as reference frames that were to be localized and oriented relative to Pol II (see Experimental Procedures and Supplemental Experimental Procedures). The TATA-TBP reference frame contained antennas NT-DNA(−23), NT-DNA(−30), and TBP-C128, whereas the upstream DNA reference frame contained antenna NT-DNA(−18). Because the structure of TFIIB in the OC is unknown, the antennas on TFIIB were treated as independent dye molecules without the assignment to a reference frame.

In the global NPS docking analysis, the complete data set consisting of mean FRET efficiencies, anisotropies, and isotropic Förster distances was used to simultaneously infer positions and orientations of all antennas and the corresponding reference frames within the Pol II coordinate system. As a result of Bayesian parameter estimation, we obtained the three-dimensional probability density of each antenna and of any desired position within the docked reference frames (Figure 5A). Comparison with the CC model derived from crosslinking data (Chen and Hahn, 2004; Chen et al., 2007; Miller and Hahn, 2006) or modeling based on X-ray crystallography (Kostrewa et al., 2009) reveals significant structural differences. Whereas TATA-DNA and TBP are located over the wall at the end of the cleft in the CC, the densities for TATA box positions are localized above the cleft between the clamp and protrusion in the OC (Figure 5A). The density of NT-DNA(−18) indicates a shift of upstream DNA into the upper cleft toward the rudder, and the density for the antenna on TBP is localized above the clamp coiled-coil.

Upstream DNA Is Stabilized by Initiation Factors

To investigate whether the observed location of the TBP-TATA DNA complex and upstream DNA results from the presence of general TFs, we compared smFRET data from the antenna NT-DNA(−30) on the TATA box to the satellite T-DNA(+7) obtained in an OC, a Pol II-DNA scaffold complex lacking factors, and an EC without factors but comprising a 17 nt RNA

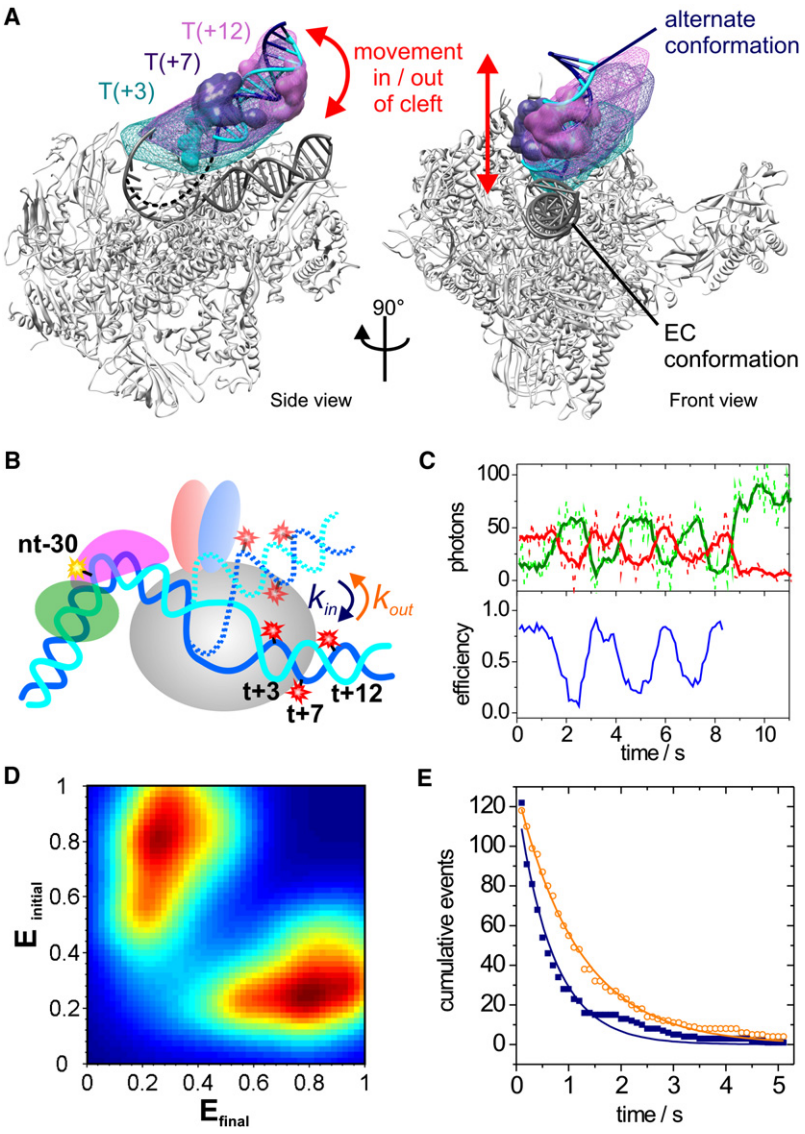

Figure 4. Downstream DNA Switches Dynamically between Positions Inside and Outside of the Cleft

(A) Global NPS localizes downstream DNA in an alternate conformation outside of the cleft. The position probability densities resulting from the global NPS analysis of the downstream DNA antennas T-DNA(+3) (dark cyan), T-DNA(+7) (dark purple), and T-DNA(+12) (orchid) are shown as meshed credible volumes contoured at 68% probability relative to the Pol II EC (Kettenberger et al., 2004). The conformation of the DNA in the EC (without RNA) is shown in gray. One possible position of the downstream DNA in the alternate conformation (non-template DNA, cyan; template DNA, blue) was modeled using Chimera (Pettersen et al., 2004). Thereby, the downstream duplex DNA (register [+3]–[+15]) was moved together with the simulated accessible volumes of the antenna dyes (solid, same color coding as for NPS densities) upwards in the cleft to match the NPS densities. To adopt the alternate conformation, the downstream DNA moves above the cleft between the Pol II clamp and lobe. During this process, part of the single-stranded template DNA upstream of T(+3) is likely to move as well (black dashed line). In the side view, Pol II Rpb9 and a major part of Rpb2 are omitted to better visualize the path of the DNA.

(B) Cartoon illustrating the two conformations of the *downstream* DNA that show dynamic inter-conversion. k_{in} is the rate for the DNA being loaded into the EC conformation (low FRET state) and k_{out} is the rate for the movement out of that conformation into the alternate conformation (high FRET state).

(C) Example of directly observed dynamic transitions between low- and high-FRET state. Time trace of fluorescence intensities (dashed lines, raw data, and solid lines, 5 point moving average) for donor NT-DNA(−30)-Tamra (green) and acceptor T-DNA(+3)-Alexa 647 (red) are shown together with the computed FRET efficiency (blue).

(D) Transition density plot (TDP) for FRET efficiency transitions from the initial FRET efficiency $E_{initial}$ to the final FRET efficiency E_{final} resulting from HMM analysis of a total of 88 traces showing 240 transitions of OCs labeled with Tamra at NT-DNA(−30) and with Alexa 647 at T-DNA(+3). HMM analysis of dynamic traces measured for OCs with NT-DNA(−30)-Tamra and T-DNA(+7)-Alexa 647 yielded similar results for the kinetics of the downstream DNA (data not shown).

(E) Cumulative distributions showing the number of transition events with a dwell time longer than a given time for the transition from low to high FRET (DNA unloading, orange circles) and for the transition from high- to low-FRET (DNA loading into cleft, blue squares) using the HMM results shown in (D). The solid lines represent the corresponding monoexponential decay fit, from which the kinetic rates k_{out} = (0.8 ± 0.1) s^{-1} and k_{in} = (1.5 ± 0.4) s^{-1} were extracted, respectively.

(Figure S6). The recorded histograms for EC and the Pol II-DNA complex were very different from the bimodal OC histogram. Both histograms covered a wide range of FRET efficiencies, from 10% to 80%, with the maximum at around 15% FRET. Thus, the examined OC is distinct from the EC regarding the location of upstream DNA, and initiation factors stabilize the new upstream DNA location. The presence of a side peak in the OC histogram is consistent with the presence of the above mentioned side peaks in measurements between downstream DNA and Rpb7 and results from dynamic loading/unloading of downstream DNA. These results show that the relocation of the upstream promoter assembly from the top of the wall to a defined position above the cleft is a consequence of the presence of the initiation factors in the OC.

Model of the OC

To build a model of the OC structure, we started from the CC model (Kostrewa et al., 2009) and used the probability densities of the antenna dye attachment points on the TATA box, TBP, and the upstream DNA, together with structural considerations (Figure 5B). Promoter DNA upstream of register −10, including TATA box and TBP, was moved as a rigid body such that the antenna attachment points on TBP, the TATA box, and NT-DNA(−18) were situated in their respective densities, and such that the connection of downstream DNA with the upstream template strand at −10, the last ordered nucleotide in the Pol II EC structure, was maintained (arrows in Figure 5A). This resulted in a clash of the upstream DNA bps (−12) – (−16) with the B-linker. We assumed that the B-linker was released from the

clamp coiled-coil in the OC, and removed it from the model. To avoid minor clashes of the nontemplate DNA nt −11 and −10 with the Pol II rudder and fork loop 1, we extended the melted region by two bases upstream. In the resulting model, re-annealing of upstream DNA strands occurs at register −12, and the backbone of nontemplate DNA at this register resides close to Rpb1 residues 313-316 in the rudder and the conserved Lys471 in Rpb2 fork loop 1. The upstream DNA duplex exits from the Pol II cleft between clamp and protrusion, generally as in the complete EC (Andrecka et al., 2009).

B-Core Is Displaced from the Wall

Because the position of both the TATA box and TBP change during the transition from CC to OC, we determined whether the position of the B-core, which mediates the attachment of TATA/TBP to the Pol II wall in the CC, changes as well. Figure 6 shows the NPS results for the antennas on TFIIB within the Pol II coordinate system, together with the model of upstream promoter DNA and TBP in the OC and the B-core in the CC model. The density for antenna TFIIB-(C-term)ybbR is located above the cleft adjacent to the TATA box and TBP on the side facing the downstream DNA. The antenna at the N-terminus of cyclin 1, TFIIB-(122)ybbR, is situated on the same DNA side but shifted toward the downstream DNA and Pol II clamp. The NPS densities show no overlap with the modeled accessible volume of the antennas in the CC model (Figure 6) and, therefore, are inconsistent with the position of the B-core in the CC as revealed by crosslinking (Chen and Hahn, 2004). Hence, the B-core is displaced from the wall in the OC but likely still interacts with DNA and TBP. To rule out that the difference in the B-core position arises from differences in measurement conditions of smFRET compared to X-ray crystallographic or crosslinking experiments, we measured smFRET between Rpb7-C150 and TFIIB-(122)ybbR within Pol II-TFIIB complexes (Figure S7). Comparison of the resulting distance with the corresponding distance in the Pol II-TFIIB crystal structure showed that the Pol II-TFIIB complex captures the same structure under both measurement conditions.

DISCUSSION

Here, we determined the three-dimensional architecture of the dynamic Pol II minimal open promoter complex, a key intermediate in transcription initiation, by smFRET analysis and modeling based on X-ray crystallographic information. In the resulting OC model, upstream promoter DNA and TBP are located above the cleft; in the CC model, they are located over the wall at the end of the cleft (Figure 7). In contrast to a prior assumption (Kostrewa et al., 2009; Liu et al., 2010), the TATA-TBP assembly is apparently released from the Pol II wall during the closed-open transition. Such a rearrangement explains the difference in electrophoretic mobility of the CC and OC (Buratowski et al., 1989; Wang et al., 1992).

Although the positions of upstream DNA and TBP are defined in the minimal OC, the position of downstream DNA switches between the cleft location, which is observed in the EC, and an intermediary state located above the cleft. The kinetic rates for this DNA loading/unloading process are fairly slow, on the order of a second, therefore presenting a major kinetic trap in the assembly process. Similar rates for DNA opening and closing were reported recently for the mitochondrial RNA polymerase of yeast Rpo41 and its transcription factor Mtf1 (Kim et al., 2012). The rate of DNA loading into the cleft might be biased by the mismatch present in the DNA scaffold and is likely to change when a fully complementary DNA is used. However, the observation that melted DNA leaves the cleft cannot be influenced by the mismatches because DNA at this point is, by definition, melted. Moreover, transcription factors not included in the minimal OC, such as TFIIE, -H, -D, or mediator, are likely to influence the observed dynamics of the downstream DNA, thereby regulating the stability and activity of the OC. We assume that additional factors shift the equilibrium between different intermediate states during the transition from CC to EC by stabilizing or destabilizing successive states. It is important to note that the observed dynamics of downstream DNA are conceivable even in the presence of additional initiation factors.

Our results have implications for the mechanism of DNA melting. Torsional stress on the DNA duplex is released during DNA melting (Strick et al., 1998), possibly involving an approximate 45° counter-clockwise rotation of the upstream DNA-TBP assembly around the TBP C2-axis, as suggested by our modeling. In vivo, DNA melting around the transcription start site is assisted by TFIIH, which has helicase activity and hydrolyzes ATP. Crosslinking studies revealed that TFIIH interacts with DNA exclusively downstream of the TSS, apparently acting as a molecular wrench that rotates downstream DNA relative to a fixed upstream promoter assembly, thereby generating torque and melting the intervening DNA (Kim et al., 2000) (Figure 7). Our results suggest that this torque, exerted by TFIIH, not only melts the DNA but also leads to a release of the upstream promoter assembly from the Pol II wall.

Our results converge with published data on a better understanding of the OC-EC transition (Figure 7). First, the course of upstream duplex DNA emanating from Pol II is similar in the OC and EC (Andrecka et al., 2009), requiring hardly any change in upstream DNA location during the OC-EC transition (Figure 7). Whereas upstream DNA is fixed in the OC, presumably due to stabilization by initiation factors, it is mobile in the EC (Andrecka et al., 2009). Second, the close proximity of the junction between upstream DNA and the transcription bubble to the rudder (Figure 5C) is consistent with the essential function of the rudder during OC formation by archaeal and bacterial RNA polymerases in vitro (Kuznedelov et al., 2002; Naji et al., 2008). Third, the upstream edge of the transcription bubble may be maintained by TFIIE, which is positioned on the clamp (Chen et al., 2007; Grohmann et al., 2011). At last, during the OC-EC transition, TFIIE is likely displaced by Spt4/5, which binds the clamp coiled-coil in the EC (Grohmann et al., 2011; Klein et al., 2011; Martinez-Rucobo et al., 2011).

Finally, our results suggest that B-core and B-linker may be displaced from the Pol II surface in the OC, indicating a stepwise release of TFIIB during the initiation-elongation transition. TFIIB remains associated with the complex, apparently via interactions of its B-ribbon and B-reader with Pol II, and aided by stabilizing interactions with TFIIF (Čabart et al., 2011). Although the many flexible connections within TFIIB prevented us from

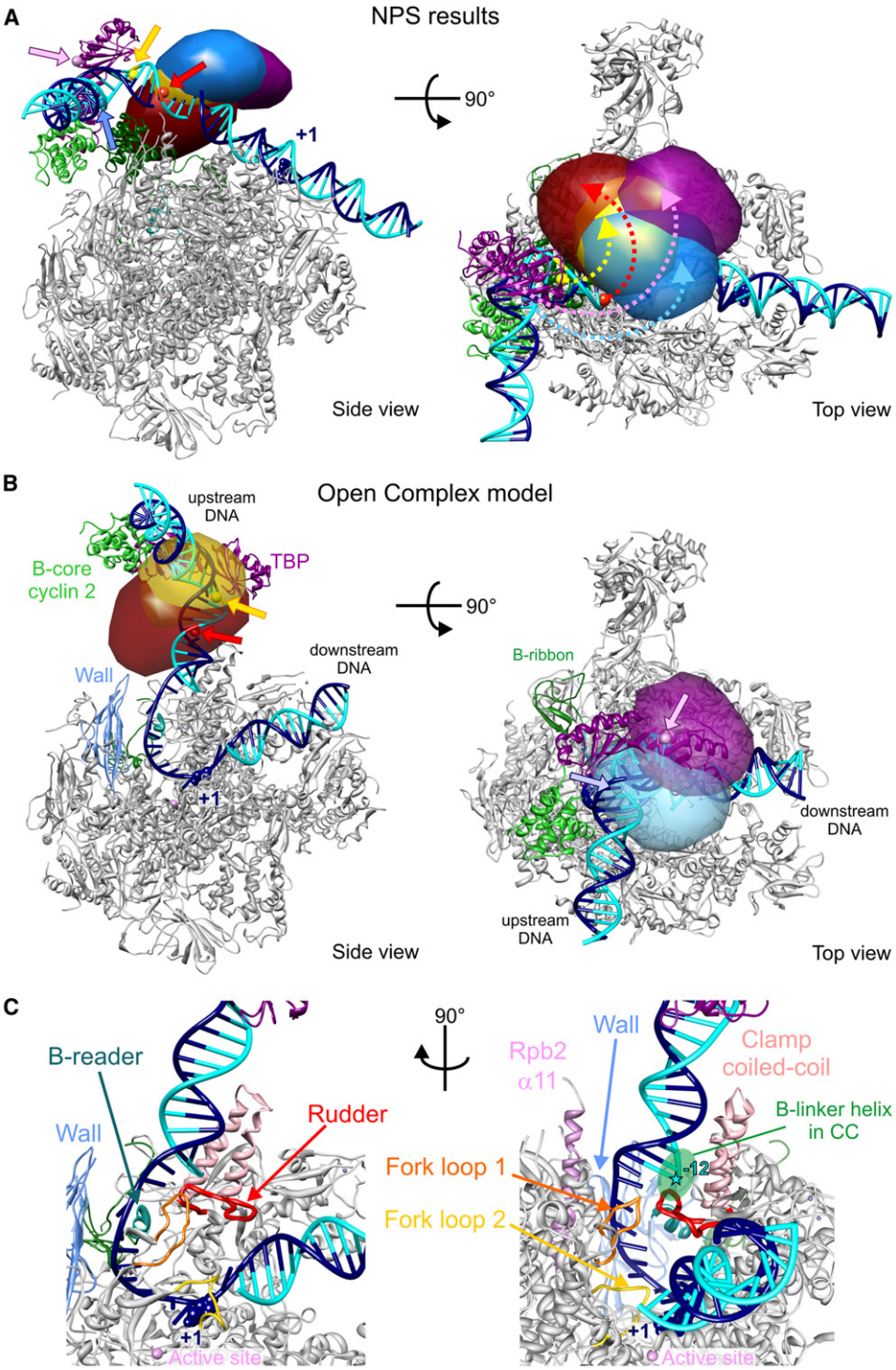

Figure 5. NPS Results for Upstream Promoter DNA and TBP and Resulting OC Model

(A) The densities of the antenna dye attachment points at NT-DNA(−18) (dark red), NT-DNA(−23) (yellow), NT-DNA(−30) (light blue), and TBP-C128 (dark magenta) within the OC, revealed by NPS, are shown as credible volumes contoured at 68% probability. The CC model (Kostrewa et al., 2009) is also shown (NT-DNA, cyan; T-DNA, blue; TBP, dark magenta; and TFIIB, green) with the TSS represented as a space-filling model. For comparison, the antenna dye attachment points on the nontemplate upstream DNA and on TBP within the CC model are shown as spheres (marked by arrows in side view) using the same color coding as for the densities. Top, arrows indicate the movement of the different antenna attachment points on DNA and TBP during the transition from CC to OC.

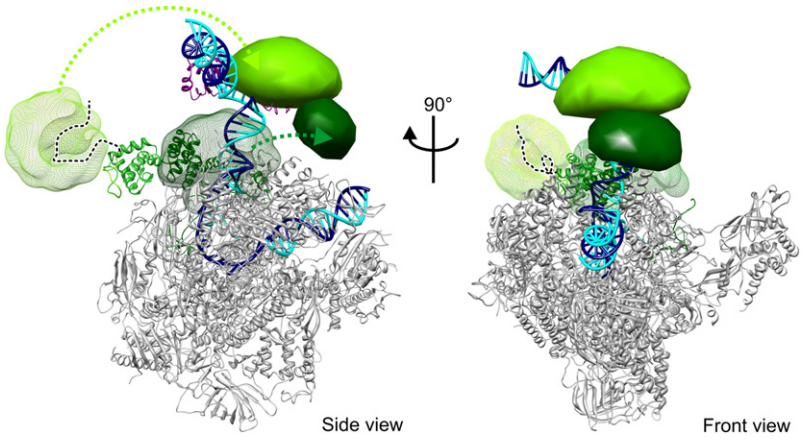

Figure 6. NPS Localization Results of TFIIB

Three-dimensional probability densities of the antenna dyes TFIIB-(122)ybbR (dark green) and TFIIB-(C-term) ybbR (light green) revealed by NPS (68% credible volumes) are shown together with the OC model of the upstream DNA and TBP and the B-core cyclin folds in the CC model in the Pol II coordinate system. The meshed volumes represent the corresponding accessible volumes of the antenna dyes within the CC model (same color coding). Because the conformation of neither the ybbR-tag nor the flexible linker connecting the dye with the ybbR-tag is known, the antenna dyes are able to access large volumes. For illustration reasons, we modeled the unknown parts of TFIIB in a possible conformation using coot (Emsley et al., 2010) and indicated them by a dashed line. Arrows indicate the rearrangement, which the two antennas need to undergo to match the NPS results. The images were prepared using Chimera (Pettersen et al., 2004). See Figure S5 for FRET efficiency histograms used in the NPS analysis.

modeling its structure within the OC, we did show that the B-core resides above the cleft and not above the wall, as in the CC. Our NPS data agree with a model in which the cyclin 2 domain of the B-core remains bound to the TATA-TBP complex as in the B-core-TATA-TBP crystal structures (Kosa et al., 1997; Nikolov et al., 1995; Tsai and Sigler, 2000) (Figures 5B and 7). In contrast, our data and modeling show that the location of the B-core cyclin 1 domain in the OC does not correspond to that observed in the crystallized B-core-TATA-TBP complex. This indicates that the two cyclin domains can move in relation to one another, consistent with NMR data (Hayashi et al., 1998). These results underline the key role of TFIIB and its intrinsic flexibility during the initiation-elongation transition and explain the experimental difficulties in structurally defining the initiation-elongation transition.

During the revision of our manuscript, a new study was published (Fishburn and Hahn, 2012) that used biochemical crosslinking to obtain information about the position of TFIIB within minimal yeast OCs. This study showed that the B-core is detached from the wall in the OC, whereas the B-ribbon and -reader remain bound to Pol II as in the CC, in agreement with the data and model presented here.

EXPERIMENTAL PROCEDURES

Protein Expression, Purification, and Labeling

Wild-type *S. cerevisiae* TBP and TFIIB were expressed and purified according to standard procedures (Supplemental Experimental Procedures). Single-cysteine mutants of TBP were prepared by site-directed mutagenesis, removing all natural cysteines and introducing a new cysteine at position 128 (S128C). Purified mutant proteins were labeled with Alexa 647 (see Supplemental Experimental Procedures). Site-specific labeling of TFIIB was achieved by the Sfp phosphopantetheinyl transferase-catalyzed ybbR-tag protein labeling technique (Yin et al., 2006) (see Supplemental Experimental Procedures).

Complex Assembly

Labeled, purified OCs were prepared by incubating recombinant TFIIB, nucleic acid scaffold, recombinant TBP, and purified endogenous *S. cerevisiae* Pol II-TFIIF (Chen et al., 2010) in assembly buffer (50 mM HEPES, 40 mM ammonium sulfate, 10 μM $ZnCl_2$, 5% glycerol, 10 mM DTT) followed by gel filtration purification. In some experiments, labeled Rpb7-C150 (Andrecka et al., 2008) was used as a satellite. Labeled Rpb4/7 was then added in 15- to 20-fold molar excess to Pol II-TFIIF to exchange unlabeled for labeled Rpb4/7. Subsequently, OC assembly was conducted as described above. To assemble OCs without TFIIF, we used purified, endogenous 12-subunit *S. cerevisiae* Pol II (Supplemental Experimental Procedures).

ECs consisted of 12-subunit Pol II and a nucleic acid scaffold containing 17 nt RNA as described previously (Andrecka et al., 2009).

SmFRET Measurements: Experimental Setup and Data Analysis

SmFRET experiments were performed on a homebuilt prism-based total internal reflection fluorescence microscope (TRIFM) as described previously (Andrecka et al., 2008) (see Supplemental Experimental Procedures).

Hidden Markov Model Analysis of Dynamic smFRET Time Traces

Dynamic smFRET time traces were selected and HMM analysis was performed using custom-written MATLAB (The MathWorks) software. The software is based on the MATLAB HMM-Toolbox by Kevin Murphy (www.cs.ubc.ca/~murphyk/Software/HMM/hmm.html) and the used algorithm is similar to one previously described for HMM analysis of time-binned smFRET trajectories (McKinney et al., 2006). A two-state hidden Markov process was assumed and an initial value for the width of states of 0.2 (20% FRET) was chosen because the Gaussian fits of the experimental FRET efficiency histograms are on average about ~ 0.2 in width. HMM analysis identified transitions between the two states in the time-binned smFRET time trajectories, and all transitions were compiled in a transition density plot (TDP) (initial versus final FRET efficiency of every transition). The different transition populations in the TDP were selected, and the cumulative events with a dwell time longer than a given time (t) were plotted against the time for each population. A single

(B) Model of the OC based on NPS results. The antenna dye attachment points of NT(−18) and NT(−23) (side view) and of NT(−30) and TBP-C128 (top) are shown as spheres together with the corresponding NPS densities as semitransparent credible volumes (NT[−18]; NT[−23], 80% probability; NT[−30]; TBP-C128, 68% probability).

(C) Pathway of DNA in the OC model entering the active center cleft. Zoom into the OC model shows structural features important for OC formation. The TSS is shown as a space-filling model. The position of the B-linker helix in the CC is indicated.

All images were prepared using Chimera (Pettersen et al., 2004). See Figures S3 and S4 for FRET efficiency histograms used in the NPS analysis.

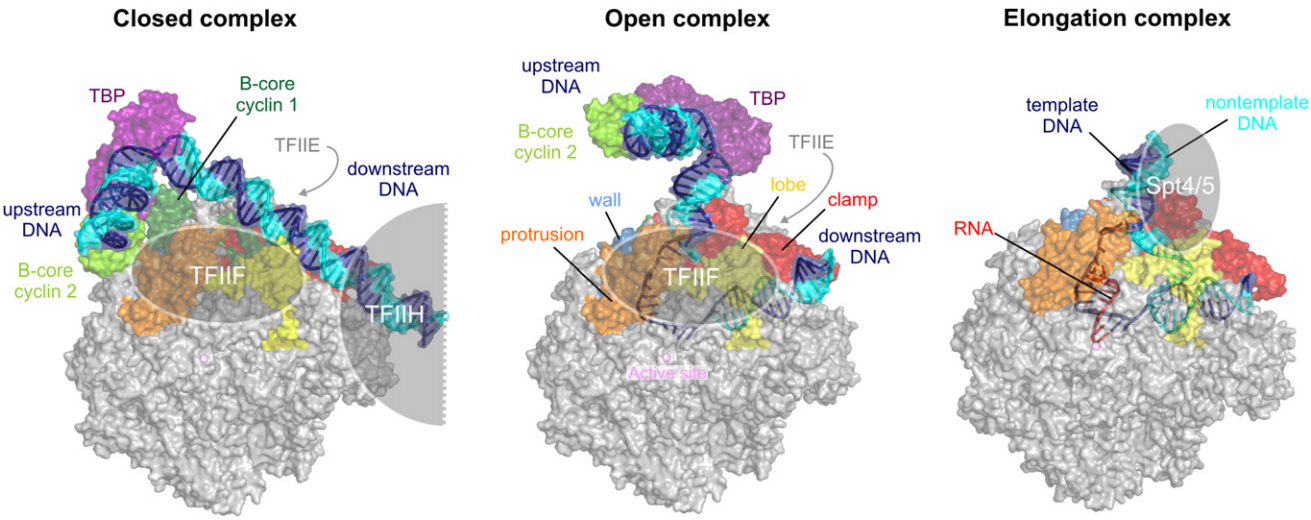

Figure 7. OC Architecture in the Context of the Initiation-Elongation Transition

CC model (Kostrewa et al., 2009) (left), OC model (middle), and complete EC model (Andrecka et al., 2009; Kettenberger et al., 2004) (right) are shown as semitransparent surface representations in the side view. Nucleic acids are additionally presented using cartoon representations. Locations of the general factors TFIIF, -IIH, and -IIE as determined by biochemical probing (Chen et al., 2007; Chen et al., 2010; Kim et al., 2000) as well as elongation factor Spt4/5 (Martinez-Rucobo et al., 2011) are indicated. All images were prepared using Pymol (The PyMOL Molecular Graphics System, Version 1.3, Schrödinger).

exponential-decay function was fitted to the cumulative distribution and the rate *k* of the transition could be extracted from the exponent.

Global NPS Analysis

Satellites were attached via flexible linkers to positions on the template DNA and on Pol II within OCs. Because the satellite attachment points did not change compared to their position within the Pol II EC (see Results), the X-ray structure of the Pol II EC (pdb ID: 1Y1W) (Kettenberger et al., 2004) was used as a reference frame. Antennas were attached via flexible linkers to positions on the upstream nontemplate DNA (NT[−18]), the TATA box (NT[−23], NT[−30]), TBP-C128, or TFIIB ([C-term]ybbR or [122]ybbR). All attachment points were unknown in the coordinate system of the Pol II EC and were to be determined therein by application of NPS. However, we used information about the local macromolecule structure because this structure is not subject to conformational change when incorporated into an OC, and we introduced reference frames for the antenna dyes (NT[−18]: pdb ID 1BNA [Drew et al., 1981], TATA-TBP: pdb ID 1VOL [Nikolov et al., 1995]). Position priors of the satellite and antenna dyes were computed by simulating the accessible volumes of the dyes relative to the respective reference structure using a flexible linker model (Figures 1B, S1, Table S3, and Supplemental Experimental Procedures). In contrast, because TFIIB is likely to adopt a conformation in the OC distinct from those in known structures (Kostrewa et al., 2009; Nikolov et al., 1995), TFIIB antenna priors were only restricted to a volume not occupied by Pol II in the EC structure (Kettenberger et al., 2004).

Bayesian parameter estimation was applied using all measured average FRET efficiencies, determined fluorescence anisotropies and Förster distances (Supplemental Experimental Procedures) to simultaneously infer position and orientation of all fluorophores within the "laboratory" coordinate system of the Pol II EC. Moreover, the information of all fluorophores linked to a reference frame were used to also position and orient the reference frame itself with respect to the Pol II EC coordinate system. As a result, we obtain the probability density function (PDF) of the position of antennas and satellites. The NPS software is available at www.uni-ulm.de/nawi/nawi-biophys.html (Muschielok and Michaelis, 2011).

After NPS analysis, the marginal position PDFs of the antenna dyes and of the attachment points of the dyes within the docked reference frames relative to the Pol II EC coordinate system were exported as XPLOR or mrc files with a resolution of 6-8 Å (see Supplemental Information). The credible volumes (i.e., the 3-dimensional error bars) of the positions were finally displayed as isosurfaces in Chimera (Pettersen et al., 2004).

Modeling

The OC model was constructed using the molecular design software Moloc (Muller et al., 1988) and its stereochemistry was optimized. Small structural changes within the Pol II structure were introduced during energy-minimization of Rpb1 residues Asp268, Lys271, Lys317 and Rpb2 residues Arg430, Gln469, Lys470.

SUPPLEMENTAL INFORMATION

Supplemental Information includes Supplemental Experimental Procedures, seven figures, and three tables and can be found with this article online at doi:10.1016/j.molcel.2012.02.008.

ACKNOWLEDGMENTS

We would like to thank A. Jasiak and J. Obel for help with protein purification and A. Cheung, S. Sainsbury, and G. Heiss for helpful discussions and materials. B.T. was supported by the Boehringer-Ingelheim-Fonds and Elitenetzwerk Bayern. P.C. was supported by the Deutsche Forschungsgemeinschaft (SFB646, TR5, FOR1068, NIM, Leibniz-Programm), the LMUinnovativ project BIN, and an ERC Advanced Investigator Grant. J.M. was supported by the Deutsche Forschungsgemeinschaft, (SFB 646), an ERC starting grant and the Nanosystems Initiative Munich.

Received: September 26, 2011
Revised: November 4, 2011
Accepted: February 10, 2012
Published online: March 15, 2012

REFERENCES

Andrecka, J., Lewis, R., Brückner, F., Lehmann, E., Cramer, P., and Michaelis, J. (2008). Single-molecule tracking of mRNA exiting from RNA polymerase II. Proc. Natl. Acad. Sci. USA *105*, 135–140.

Andrecka, J., Treutlein, B., Arcusa, M.A., Muschielok, A., Lewis, R., Cheung, A.C., Cramer, P., and Michaelis, J. (2009). Nano positioning system reveals the course of upstream and nontemplate DNA within the RNA polymerase II elongation complex. Nucleic Acids Res. *37*, 5803–5809.

Armache, K.J., Mitterweger, S., Meinhart, A., and Cramer, P. (2005). Structures of complete RNA polymerase II and its subcomplex, Rpb4/7. J. Biol. Chem. *280*, 7131–7134.

Boeger, H., Bushnell, D.A., Davis, R., Griesenbeck, J., Lorch, Y., Strattan, J.S., Westover, K.D., and Kornberg, R.D. (2005). Structural basis of eukaryotic gene transcription. FEBS Lett. *579*, 899–903.

Buratowski, S., Hahn, S., Guarente, L., and Sharp, P.A. (1989). Five intermediate complexes in transcription initiation by RNA polymerase II. Cell *56*, 549–561.

Bushnell, D.A., Westover, K.D., Davis, R.E., and Kornberg, R.D. (2004). Structural basis of transcription: an RNA polymerase II-TFIIB cocrystal at 4.5 Angstroms. Science *303*, 983–988.

Čabart, P., Újvári, A., Pal, M., and Luse, D.S. (2011). Transcription factor TFIIF is not required for initiation by RNA polymerase II, but it is essential to stabilize transcription factor TFIIB in early elongation complexes. Proc Natl Acad Sci USA *108*, 15786–15791.

Chen, H.T., and Hahn, S. (2003). Binding of TFIIB to RNA polymerase II: Mapping the binding site for the TFIIB zinc ribbon domain within the preinitiation complex. Mol. Cell *12*, 437–447.

Chen, H.T., and Hahn, S. (2004). Mapping the location of TFIIB within the RNA polymerase II transcription preinitiation complex: a model for the structure of the PIC. Cell *119*, 169–180.

Chen, H.T., Warfield, L., and Hahn, S. (2007). The positions of TFIIF and TFIIE in the RNA polymerase II transcription preinitiation complex. Nat. Struct. Mol. Biol. *14*, 696–703.

Chen, Z.A., Jawhari, A., Fischer, L., Buchen, C., Tahir, S., Kamenski, T., Rasmussen, M., Lariviere, L., Bukowski-Wills, J.C., Nilges, M., et al. (2010). Architecture of the RNA polymerase II-TFIIF complex revealed by cross-linking and mass spectrometry. EMBO J. *29*, 717–726.

Cheung, A.C.M., Sainsbury, S., and Cramer, P. (2011). Structural basis of initial RNA polymerase II transcription. EMBO J. *30*, 4755–4763.

Cho, E.J., and Buratowski, S. (1999). Evidence that transcription factor IIB is required for a post-assembly step in transcription initiation. J. Biol. Chem. *274*, 25807–25813.

Cramer, P., Bushnell, D.A., and Kornberg, R.D. (2001). Structural basis of transcription: RNA polymerase II at 2.8 angstrom resolution. Science *292*, 1863–1876.

Drew, H.R., Wing, R.M., Takano, T., Broka, C., Tanaka, S., Itakura, K., and Dickerson, R.E. (1981). Structure of a B-DNA dodecamer: conformation and dynamics. Proc. Natl. Acad. Sci. USA *78*, 2179–2183.

Emsley, P., Lohkamp, B., Scott, W.G., and Cowtan, K. (2010). Features and development of Coot. Acta Crystallogr. D Biol. Crystallogr. *66*, 486–501.

Fishburn, J., and Hahn, S. (2012). Architecture of the yeast RNA polymerase II open complex and regulation of activity by TFIIF. Mol. Cell. Biol. *32*, 12–15.

Giardina, C., and Lis, J.T. (1993). DNA melting on yeast RNA polymerase II promoters. Science *261*, 759–762.

Gnatt, A.L., Cramer, P., Fu, J., Bushnell, D.A., and Kornberg, R.D. (2001). Structural basis of transcription: an RNA polymerase II elongation complex at 3.3 A resolution. Science *292*, 1876–1882.

Grohmann, D., Nagy, J., Chakraborty, A., Klose, D., Fielden, D., Ebright, R.H., Michaelis, J., and Werner, F. (2011). The initiation factor TFE and the elongation factor Spt4/5 compete for the RNAP clamp during transcription initiation and elongation. Mol. Cell *43*, 263–274.

Ha, T., Enderle, T., Ogletree, D.F., Chemla, D.S., Selvin, P.R., and Weiss, S. (1996). Probing the interaction between two single molecules: fluorescence resonance energy transfer between a single donor and a single acceptor. Proc. Natl. Acad. Sci. USA *93*, 6264–6268.

Hahn, S. (2004). Structure and mechanism of the RNA polymerase II transcription machinery. Nat. Struct. Mol. Biol. *11*, 394–403.

Hayashi, F., Ishima, R., Liu, D., Tong, K.I., Kim, S., Reinberg, D., Bagby, S., and Ikura, M. (1998). Human general transcription factor TFIIB: conformational variability and interaction with VP16 activation domain. Biochemistry *37*, 7941–7951.

Joo, C., Balci, H., Ishitsuka, Y., Buranachai, C., and Ha, T. (2008). Advances in single-molecule fluorescence methods for molecular biology. Annu. Rev. Biochem. *77*, 51–76.

Kettenberger, H., Armache, K.J., and Cramer, P. (2004). Complete RNA polymerase II elongation complex structure and its interactions with NTP and TFIIS. Mol. Cell *16*, 955–965.

Killeen, M., Coulombe, B., and Greenblatt, J. (1992). Recombinant TBP, transcription factor IIB, and RAP30 are sufficient for promoter recognition by mammalian RNA polymerase II. J. Biol. Chem. *267*, 9463–9466.

Kim, T.K., Ebright, R.H., and Reinberg, D. (2000). Mechanism of ATP-dependent promoter melting by transcription factor IIH. Science *288*, 1418–1422.

Kim, H., Tang, G.Q., Patel, S.S., and Ha, T. (2012). Opening-closing dynamics of the mitochondrial transcription pre-initiation complex. Nucleic. Acids Res. *40*, 371–380.

Klein, B.J., Bose, D., Baker, K.J., Yusoff, Z.M., Zhang, X., and Murakami, K.S. (2011). RNA polymerase and transcription elongation factor Spt4/5 complex structure. Proc. Natl. Acad. Sci. USA *108*, 546–550.

Knight, J.L., Mekler, V., Mukhopadhyay, J., Ebright, R.H., and Levy, R.M. (2005). Distance-restrained docking of rifampicin and rifamycin SV to RNA polymerase using systematic FRET measurements: developing benchmarks of model quality and reliability. Biophys. J. *88*, 925–938.

Kosa, P.F., Ghosh, G., DeDecker, B.S., and Sigler, P.B. (1997). The 2.1-A crystal structure of an archaeal preinitiation complex: TATA-box-binding protein/transcription factor (II)B core/TATA-box. Proc. Natl. Acad. Sci. USA *94*, 6042–6047.

Kostrewa, D., Zeller, M.E., Armache, K.J., Seizl, M., Leike, K., Thomm, M., and Cramer, P. (2009). RNA polymerase II-TFIIB structure and mechanism of transcription initiation. Nature *462*, 323–330.

Kuznedelov, K., Korzheva, N., Mustaev, A., and Severinov, K. (2002). Structure-based analysis of RNA polymerase function: the largest subunit's rudder contributes critically to elongation complex stability and is not involved in the maintenance of RNA-DNA hybrid length. EMBO J. *21*, 1369–1378.

Liu, X., Bushnell, D.A., Wang, D., Calero, G., and Kornberg, R.D. (2010). Structure of an RNA polymerase II-TFIIB complex and the transcription initiation mechanism. Science *327*, 206–209.

Margittai, M., Widengren, J., Schweinberger, E., Schröder, G.F., Felekyan, S., Haustein, E., König, M., Fasshauer, D., Grubmüller, H., Jahn, R., and Seidel, C.A. (2003). Single-molecule fluorescence resonance energy transfer reveals a dynamic equilibrium between closed and open conformations of syntaxin 1. Proc. Natl. Acad. Sci. USA *100*, 15516–15521.

Martinez-Rucobo, F.W., Sainsbury, S., Cheung, A.C., and Cramer, P. (2011). Architecture of the RNA polymerase-Spt4/5 complex and basis of universal transcription processivity. EMBO J. *30*, 1302–1310.

McKinney, S.A., Joo, C., and Ha, T. (2006). Analysis of single-molecule FRET trajectories using hidden Markov modeling. Biophys. J. *91*, 1941–1951.

Mekler, V., Kortkhonjia, E., Mukhopadhyay, J., Knight, J., Revyakin, A., Kapanidis, A.N., Niu, W., Ebright, Y.W., Levy, R., and Ebright, R.H. (2002). Structural organization of bacterial RNA polymerase holoenzyme and the RNA polymerase-promoter open complex. Cell *108*, 599–614.

Miller, G., and Hahn, S. (2006). A DNA-tethered cleavage probe reveals the path for promoter DNA in the yeast preinitiation complex. Nat. Struct. Mol. Biol. *13*, 603–610.

Muller, K., Amman, H.J., Doran, D.M., Gerber, P.R., Gubernator, K., and Schrepfer, G. (1988). MOLOC: A molecular modeling program. Bull. Soc. Chim. Belg. *97*, 655–667.

Muschielok, A., and Michaelis, J. (2011). Application of the nano-positioning system to the analysis of fluorescence resonance energy transfer networks. J. Phys. Chem. B *115*, 11927–11937.

Muschielok, A., Andrecka, J., Jawhari, A., Brückner, F., Cramer, P., and Michaelis, J. (2008). A nano-positioning system for macromolecular structural analysis. Nat. Methods *5*, 965–971.

Naji, S., Bertero, M.G., Spitalny, P., Cramer, P., and Thomm, M. (2008). Structure-function analysis of the RNA polymerase cleft loops elucidates initial transcription, DNA unwinding and RNA displacement. Nucleic Acids Res. *36*, 676–687.

Nikolov, D.B., Chen, H., Halay, E.D., Usheva, A.A., Hisatake, K., Lee, D.K., Roeder, R.G., and Burley, S.K. (1995). Crystal structure of a TFIIB-TBP-TATA-element ternary complex. Nature *377*, 119–128.

Pal, M., Ponticelli, A.S., and Luse, D.S. (2005). The role of the transcription bubble and TFIIB in promoter clearance by RNA polymerase II. Mol. Cell *19*, 101–110.

Pan, G., and Greenblatt, J. (1994). Initiation of transcription by RNA polymerase II is limited by melting of the promoter DNA in the region immediately upstream of the initiation site. J. Biol. Chem. *269*, 30101–30104.

Pardee, T.S., Bangur, C.S., and Ponticelli, A.S. (1998). The N-terminal region of yeast TFIIB contains two adjacent functional domains involved in stable RNA polymerase II binding and transcription start site selection. J. Biol. Chem. *273*, 17859–17864.

Pettersen, E.F., Goddard, T.D., Huang, C.C., Couch, G.S., Greenblatt, D.M., Meng, E.C., and Ferrin, T.E. (2004). UCSF Chimera—a visualization system for exploratory research and analysis. J. Comput. Chem. *25*, 1605–1612.

Ranish, J.A., Yudkovsky, N., and Hahn, S. (1999). Intermediates in formation and activity of the RNA polymerase II preinitiation complex: holoenzyme recruitment and a postrecruitment role for the TATA box and TFIIB. Genes Dev. *13*, 49–63.

Rasnik, I., Myong, S., Cheng, W., Lohman, T.M., and Ha, T. (2004). DNA-binding orientation and domain conformation of the E. coli rep helicase monomer bound to a partial duplex junction: single-molecule studies of fluorescently labeled enzymes. J. Mol. Biol. *336*, 395–408.

Roeder, R.G. (1996). The role of general initiation factors in transcription by RNA polymerase II. Trends Biochem. Sci. *21*, 327–335.

Strick, T.R., Allemand, J.F., Bensimon, D., and Croquette, V. (1998). Behavior of supercoiled DNA. Biophys. J. *74*, 2016–2028.

Tsai, F.T., and Sigler, P.B. (2000). Structural basis of preinitiation complex assembly on human pol II promoters. EMBO J. *19*, 25–36.

Wang, W., Carey, M., and Gralla, J.D. (1992). Polymerase II promoter activation: closed complex formation and ATP-driven start site opening. Science *255*, 450–453.

Wang, D., Bushnell, D.A., Westover, K.D., Kaplan, C.D., and Kornberg, R.D. (2006). Structural basis of transcription: role of the trigger loop in substrate specificity and catalysis. Cell *127*, 941–954.

Wozniak, A.K., Schröder, G.F., Grubmüller, H., Seidel, C.A., and Oesterhelt, F. (2008). Single-molecule FRET measures bends and kinks in DNA. Proc. Natl. Acad. Sci. USA *105*, 18337–18342.

Yin, J., Lin, A.J., Golan, D.E., and Walsh, C.T. (2006). Site-specific protein labeling by Sfp phosphopantetheinyl transferase. Nat. Protoc. *1*, 280–285.